CHEMISTRY OF MATERIALS

pubs.acs.org/cm

Article

Less Is More: Simplified Fluorene-Based Dopant-Free Hole Transport Materials Promote the Long-Term Ambient Stability of Perovskite Solar Cells

Paavo Mäkinen, Francesca Fasulo, Maning Liu, G. Krishnamurthy Grandhi, Daniele Conelli, Basheer Al-Anesi, Harri Ali-Löytty, Kimmo Lahtonen, Sami Toikkonen, Gian Paolo Suranna, Ana Belén Muñoz-García, Michele Pavone, Roberto Grisorio,* and Paola Vivo*

Cite This: *Chem. Mater.* 2023, 35, 2975−2987

Read Online

ACCESS | Metrics & More | Article Recommendations | Supporting Information

ABSTRACT: The stability of perovskite solar cells (PSCs) is greatly affected by the interface between the perovskite active layer and the hole transport material (HTM). The rational design of HTMs with effective anchoring to the perovskite surface is an emerging elegant strategy to promote compact and ordered interfaces that lead to highly efficient and stable PSCs. Herein, we propose two fluorene-based HTM molecular architectures (**SCF1** and **SCF2**) derived from the popular yet expensive Spiro-OMeTAD. Their employment as dopant-free HTMs in standard triple-cation CsFAMA PSCs leads to superior device stability, with a T_{80} lifetime well above 1 year (431 days). Our combined theoretical and experimental study of the CsFAMA|HTM interface reveals that the improved adhesion of the **SCF**-HTMs to the perovskite layer is the key to minimize the non-radiative recombination, reduce the hole trap density, and enhance the long-term stability of the corresponding devices. The simplified structures of **SCF1** and **SCF2**, obtained by removing the orthogonal fragment of the Spiro-OMeTAD scaffold, show a lower molecular distortion than Spiro-OMeTAD, thus promoting a favorable electronic interaction between the **SCF**-HTMs and the perovskite. This study provides useful design criteria for achieving highly stable PSCs including dopant-free HTMs with optimized adhesion to the perovskite surface.

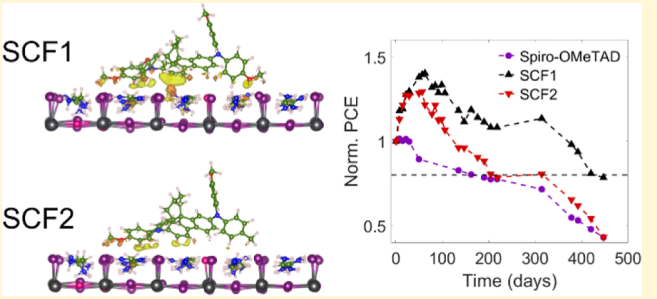

1. INTRODUCTION

The rapid development of halide perovskite solar cells (PSCs) has currently led to a certified power conversion efficiency (PCE) of 25.7%, i.e., comparable to that of silicon photovoltaics, which have been investigated already for many decades.[1] Nevertheless, the modest stability of PSCs in ambient conditions, which still limits their widespread adoption, overshadows the continuous progress on the performance and fabrication sides. The interfaces between the perovskite layer and the neighboring charge transport materials play a significant role in the longevity of PSCs[2,3] as the electron transport materials (ETMs) and hole transport materials (HTMs) act as protective layers for the perovskite. Furthermore, the chemical interactions at the perovskite interface may either promote long lifetimes (e.g., via defect passivation) or cause further instability.[4,5] Within the last few years, dozens of HTM designs for PSCs have been reported, with the aim of providing valid alternatives to 2,2′,7,7′-tetrakis(*N*,*N*-di-*p*-methoxyphenyl-amine)-9,9′-spirobifluorene (Spiro-OMeTAD) and poly[bis(4-phenyl)(2,4,6-trimethylphenyl)amine] HTMs, which are largely adopted in high-PCE devices with n−i−p and p−i−n structures, respectively.[6,7] Indeed, these well-known HTMs are costly, needing demanding syntheses in harsh conditions and requiring (especially Spiro-OMeTAD) hygroscopic dopants (namely, lithium bis(trifluoromethanesulfonyl)imide, LiTFSI, and *tert*-butylpyridine, *t*BP) to maximize their hole mobility and conductivity. For this reason, they are detrimental to the long-term stability of the devices. The community has so far mostly focused on new HTM designs as stand-alone layers in PSCs, i.e., targeting molecules with high intrinsic mobility and conductivity (thus being potentially good dopant-free layers) and appropriate energy-level alignment to maximize charge extraction and reduce open-circuit voltage (V_{OC}) losses.[7] Only recently, the idea of tailoring specific chemical interactions between the perovskite and the HTM has been exploited, with designs that combine the HTM function with the formation of

Received: January 23, 2023
Revised: March 3, 2023
Published: March 14, 2023

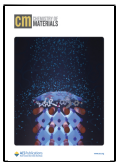

Figure 1. Chemical structures of **SCF1** and **SCF2** in comparison with that of Spiro-OMeTAD.

compact and ordered interfaces with the perovskite, in turn significantly boosting the PSC stability.[8−13] However, the identification of a competitive alternative to the traditional Spiro-OMeTAD HTM that would enable remarkable long-term stability of PSCs in ambient conditions, while at the same time guaranteeing simple synthetic protocols and low material consumption, is still a hot topic and requires further attention.[14−16] Only an in-depth rationalization of the complex phenomena occurring at the perovskite|HTM interface could provide new criteria in designing HTMs for efficient and, more importantly, stable PSCs.

In this study, we analyze the role of the adhesion between the HTM and the perovskite surface in the long-term PSC stability by comparing the behavior of traditional Spiro-OMeTAD with simplified structures derived from it (named **SCF1** and **SCF2**, see Figure 1). These novel HTMs are designed by eliminating the orthogonal portion of the Spiro-OMeTAD scaffold to reduce the molecular distortion required for the surface anchoring. Independently of the peripheral functional groups ($-OCH_3$ or $-CH_3$ for **SCF1** and **SCF2**, respectively), they possess suitable energy levels for charge extraction from the perovskite layer, good thermal stability, hydrophobicity, as well as comparable hole mobility to undoped Spiro-OMeTAD, yet at a fraction of its synthetic sequence. When SCF-HTMs were employed as thin layers (more than 3 times thinner than the traditional HTMs) in *n*−*i*−*p* structured PSCs with the triple-cation halide perovskite $Cs_{0.05}(FA_{0.83}\ MA_{0.17})_{0.95}Pb(I_{0.83}Br_{0.17})_3$ (CsFAMA), the champion **SCF1**-based devices displayed an impressive shelf stability with a T_{80} lifetime of 431 days. Our theoretical study on the CsFAMA|HTM interfaces supports the enhanced stability of **SCF1** devices versus the **SCF2** and Spiro-OMeTAD counterparts as **SCF1** exhibits the highest computed binding energies.

This work highlights the importance of customizing the chemical anchoring of the HTM to the perovskite surface to enable ordered and stable interfaces. Furthermore, the significance of long-term device stability studies (e.g., >1 year) when assessing a new HTM is emphasized, as for any practical application, the performance over time is more meaningful than that of the as-fabricated devices.

2. EXPERIMENTAL SECTION

2.1. Synthesis of the Hole-Transporting Materials. Reagents and solvents were purchased from standard commercial sources (Aldrich and Honeywell Riedel-de-Haën, respectively), while chemical manipulations were carried out under an inert nitrogen atmosphere using standard Schlenk techniques. The reaction courses were monitored by thin-layer chromatography on Merck silica gel 60 F254 aluminum sheets. NMR spectra were recorded on a Bruker AVANCE DPX 300 MHz instrument, while electrospray ionization-mass spectrometry (ESI-MS) spectra were obtained using an AB SCIEX Triple Quad 5500 instrument. Further details on the synthesis of the proposed HTMs (**SCF1** and **SCF2**) are reported in the Supporting Information , along with ^1H and ^{13}C NMR spectra (Figures S1−S4), ESI-MS study (Figures S5 and S6), and a cost analysis of the materials.

2.2. Spectroscopic and Thermal Characterization. UV−vis spectra were recorded in *o*-dichlorobenzene solutions ($\sim 10^{-5}$ M) on a JASCO V-670 instrument. Thermogravimetric analysis (TGA) was carried out on a PerkinElmer Pyris 6 TGA instrument under a nitrogen flow (40 mL/min) at a heating rate of 10 °C/min. Differential scanning calorimetry (DSC) was recorded on a Q2000 TA instrument under a nitrogen flow (50 mL/min) at a temperature scan of 10 °C/min.

2.3. Electrochemical Characterization. Cyclic voltammetry experiments were carried out on a Metrohm Autolab PGSTAT 302-N potentiostat in dichloromethane (HTM concentration: $\sim 10^{-4}$ M) containing tetrabutylammonium tetrafluoroborate (0.10 M) as the supporting electrolyte at a 100 mV/s scan rate. The potentials were measured with respect to a Ag/Ag^+ quasi-reference electrode that was calibrated against ferrocene (Fc) after each experiment. The evaluation of the highest occupied molecular orbital (HOMO) energy level of the HTMs was carried out by measuring the onset of the half-wave potential of the anodic event. The HOMO and lowest unoccupied molecular orbital (LUMO) energy levels were calculated according to eqs 1 and 2

$$E_{HOMO} = -[E_{ox} - E_{(Fc/)} + 5.10]\ (eV) \quad (1)$$

$$E_{LUMO} = E_{HOMO} + E_g\ (eV) \quad (2)$$

where $E_{(Fc/Fc^+)}$ represents the half-wave potential of the Fc/Fc^+ couple, E_{ox} represents the half-wave potential of the HTM/HTM^+ couple, and E_g corresponds to the optical band gap calculated by $E_g = 1240/\lambda_{onset}$ (eV) (where λ_{onset} represents the onset of the HTM's absorption curve recorded in solution).

2.4. Computational Study. The analyses of the ground-state geometries of the proposed HTMs were carried out by density functional theory (DFT) calculations using the B3LYP functional in conjunction with the 6-31G(d,p) basis set on isolated molecules. Calculated energies of the relevant molecules along with their optimized geometries were carried out with the 6-311G(d,p) basis set including solvent effects (conductor-like polarizable continuum model method, CH_2Cl_2). These theoretical calculations have been carried out using the Gaussian 09 program package.

The methods used for the theoretical analysis of the perovskite|HTM interface are detailed in Section 3.1 and the Supporting Information.

https://doi.org/10.1021/acs.chemmater.3c00145
Chem. Mater. 2023, 35, 2975−2987

2.5. Charge Transport Characterization. The hole mobility of HTM films was measured by employing the space−charge-limited current (SCLC) method. For this purpose, typical hole-only devices were fabricated in a structure of "glass/ITO/PEDOT:PSS/HTM/MoO_3/Au". The devices were characterized by acquiring the dark current density (J)−voltage (V^2) curves under forward bias, and the hole mobility was extracted using the Mott−Gurney law, presented in eq 3

$$J_D = \frac{9}{8}\epsilon_r\epsilon_0\mu_h\frac{V^2}{d^3} \tag{3}$$

where J_D is the dark current density, ϵ_r is the relative permittivity of the material, which is ≈3 for organic materials, ϵ_0 is the vacuum permittivity, which is 8.854×10^{-12} C V^{-1} m^{-1}, μ_h is the hole mobility, V is the applied bias, and d is the thickness of the HTM layer. The measurement was conducted with a Keithley 2450 source measure unit (SMU) between 0 and 2 V at a scan rate of 0.1 V s^{-1}, and a linear fit was applied to data points below 50 mA cm^{-2} (see Figure S7a).

Conductivity was assessed by measuring the resistance of 100 nm HTM films on glass with four equally spaced 100 nm-thick Au lines evaporated on top as electrodes. Current was sourced through the outer electrodes with the Keithley 2450 SMU, and the voltage drop between the inner electrodes was measured to calculate resistance R from a linear fit on a voltage (V)−current (I) curve (Figure S7b). Conductivity was then calculated using eq 4

$$\sigma = \frac{d}{RA} \tag{4}$$

where σ is the conductivity of the film, d is the distance between electrodes, and A is the cross-sectional area through which the current is transmitted.

2.6. X-ray Photoelectron Spectroscopy. X-ray photoelectron spectroscopy (XPS) measurements were performed under ultra-high vacuum employing an Al Kα X-ray source ($h\nu$ = 1486.7 eV) and an Argus electron spectrometer (Omicron Nanotechnology GmbH). The spectrometer binding energy scale was calibrated by setting Ag $3d_{5/2}$ of metallic Ag foil to 368.0 eV. To probe the HTM−perovskite interaction, low concentration of HTMs (0.25 mg mL^{-1} in chlorobenzene) was used in the spin coating instead of the concentration (10 mg mL^{-1}) optimized for solar cell performance. The thickness of the HTM layer scales with the concentration, and the use of low concentration allowed probing of the HTM−perovskite interface by surface-sensitive XPS (an information depth of 5−9 nm). The chemical states of elements were determined from the XPS spectra by least-squares fitting of synthetic line shapes after background subtraction. The analysis was performed in CasaXPS software version 2.3.25PR1.0.[17]

2.7. Photoluminescence and Hole Trap Density Studies. A batch of **glass/CsFAMA** and **glass/CsFAMA/HTM** samples (CsFAMA is the standard triple-cation $Cs_{0.05}(FA_{0.83}MA_{0.17})_{0.95}Pb(I_{0.83}Br_{0.17})_3$ perovskite) was prepared for the photoluminescence (PL) studies with both SCF-HTMs and doped Spiro-OMeTAD. The same cleaning and spin coating protocols were used as with solar cell fabrication, except that the glass substrates were plasma-cleaned prior to perovskite deposition. Steady-state PL spectra were recorded with a FLS1000 spectrofluorometer (Edinburgh Instruments, UK). The time-resolved PL (TRPL) decays were obtained by using a time-correlated single-photon counting apparatus equipped with a Picoharp 300 controller and a PDL 800-B driver for excitation and a Hamamatsu R3809U-50 microchannel plate photomultiplier for detection in 90° configuration. The equations used to analyze the results are presented in the Supporting Information.

Additionally, we quantified the hole trap density on the perovskite surface by fabricating hole-only devices with the structure "ITO|PEDOT:PSS|CsFAMA|HTM|MoO_3|Au".[18,19] The J−V curves of these devices were then measured in darkness, as shown in Figure S10. The applied voltage at the kink point is referred to as the trap-filled limit voltage (V_{TFL}), which can be used to calculate the trap density (N_{trap})[19] according to the following equation

$$N_{trap} = \frac{2\epsilon\epsilon_0 V_{TFL}}{eL^2} \tag{5}$$

where e is the elementary charge, L is the thickness of the perovskite layer (approximately 500 nm in our work), ϵ is the relative dielectric constant of the perovskite, and ϵ_0 is the vacuum permittivity.

2.8. Solar Cell Fabrication. All reagents and solvents aside from the SCF-HTMs were purchased from standard commercial sources and used as received. Unless specified otherwise, processes were performed in air. The solar cells were fabricated on fluorine-doped tin oxide (FTO) glass substrates (TEC 15, Greatcell Solar) with dimensions 20 × 20 × 2.2 mm, which were wet chemically etched on one edge with a 2.4 M HCl solution and zinc powder. The etched substrates were cleaned with 2% Mucasol solution in deionized water and sonicated in deionized water, acetone, and 2-propanol for 15 min each, followed by swiftly drying under a N_2 stream. A compact TiO_2 layer (c-TiO_2) was deposited on the substrates via spray pyrolysis at 450 °C using N_2 as the carrier gas. The precursor solution was prepared by diluting a titanium diisopropoxide bis(acetylacetonate) stock solution (75% in 2-propanol, Sigma-Aldrich) further to 17.3 vol %. Twelve layers of the precursor solution (<8 mL) were sprayed on the substrates with 20 s between each cycle, followed by sintering at 450 °C in air for a minimum of 45 min. A mesoporous TiO_2 (m-TiO_2) scaffold layer was deposited by spin coating an ethanolic suspension of 30 NRD TiO_2 nanoparticle paste (Greatcell Solar), with 150 mg of paste in 1 mL of ethanol. 80 μL of the suspension was spin-coated at 4000 rpm for 10 s, followed by a few minutes of annealing at 100 °C prior to calcination at 450 °C for 30 min (heat ramped over ∼45 min). The substrates were then cooled down to 150 °C and transferred to a nitrogen-filled glovebox for perovskite and HTM deposition.

The CsFAMA perovskite precursor was prepared before 24−48 h, comprising FAI (0.95 M, Greatcell Solar Materials), MABr (0.19 M, Greatcell Solar Materials), $PbBr_2$ (1.1 M, TCI), PbI_2 (0.20 M, TCI), and CsI (0.06 M, abcr) in a mixed solvent of DMSO/DMF (1:4 volume ratio). The solution was kept under stirring until use. 50 μL of the solution was spin-coated onto the as-prepared FTO/c-TiO_2/m-TiO_2 substrates at 1000 rpm for 10 s, followed by 6000 rpm for 20 s. Antisolvent treatment was carried out by dropping 100 μL of chlorobenzene onto the substrate 5 s prior to the end of the program. The perovskite films were immediately transferred to a hot plate for annealing at 110 °C for 1 h. After annealing and cooling down, the SCF-HTMs and reference-doped Spiro-OMeTAD were dynamically spin-coated on top of the perovskite film at 1800 rpm for 40 s. SCF-HTMs were tested in four concentrations (5, 10, 15, and 20 mg/mL in chlorobenzene), with 10 mg/mL yielding the highest performance. The doped Spiro-OMeTAD solution was prepared by dissolving Spiro-OMeTAD (Lumtec) in chlorobenzene in a 29.5 mM concentration and stirring at 60 °C for a few minutes. After cooling down the dopants were added 4-*tert*-butylpyridine (Sigma-Aldrich), Li-TFSI (Sigma-Aldrich, pre-dissolved in acetonitrile 520 mg/mL), and FK209 (Dyenamo, pre-dissolved in acetonitrile 300 mg/mL). Their molar equivalents to Spiro-OMeTAD were 3.2, 0.53, and 0.1, respectively. After HTM deposition, the samples were removed from the glovebox and kept in a dry cabinet overnight. Finally, 100 nm-thick gold electrodes were evaporated on top of the HTM layer using an Edwards Auto 306 vacuum deposition unit under the vacuum of approximately 10^{-5} mbar.

2.9. Device and Film Characterization. The unencapsulated PSCs, with an active area of 20 mm^2, were characterized in air. The current density (J)−voltage (V) curves were recorded at a scan rate of 50 mV s^{-1} with a Keithley 2450 SMU (controlled by a measurement program written in MATLAB) and a SS150-AAA solar simulator (Sciencetech, Canada) under air mass 1.5 simulated sunlight (100 mW cm^{-2}), calibrated with a KG5 reference cell and meter (Newport, USA). The same setup was also used for recording dark J−V behavior.

https://doi.org/10.1021/acs.chemmater.3c00145
Chem. Mater. 2023, 35, 2975−2987

Table 1. Thermal, Optical, and Electrochemical Properties of the Synthesized HTM

HTM	T_{dec} [a] (°C)	T_g [a] (°C)	λ_{max} [b] (nm)	E_g [c] (eV)	$HOMO_{DFT}$ [d] (eV)	$LUMO_{DFT}$ [d] (eV)	$HOMO_{exp}$ [e] (eV)	$LUMO_{exp}$ [f] (eV)	μ_h [g] ($cm^2\ V^{-1}\ s^{-1}$)	σ [h] (S cm^{-1})
SCF1	389	80	388	2.99	−4.69	−1.14	−4.97	−1.98	5.7×10^{-5}	1.5×10^{-6}
SCF2	370	84	387	3.02	−4.79	−1.20	−5.03	−2.01	3.6×10^{-5}	5.7×10^{-7}

[a]Decomposition (T_{dec}, 5% weight loss) and glass-transition (T_g) temperatures recorded by TGA and DSC measurements, respectively (10 °C/min, N_2 atmosphere). [b]Absorption maxima measured in CH_2Cl_2 solution (10^{-5} M). [c]Optical band gap $E_g = 1240/\lambda_{onset}$ (eV). [d]Calculated at the B3LYP/6-311G(d,p)/CPCM(CH_2Cl_2) level of theory. [e]Determined by cyclic voltammetry with the equation: exp HOMO = $-[E_{ox} - E(Fc/Fc^+) + 5.10]$ (eV). [f]exp LUMO = exp HOMO + E_g (eV). [g]Average hole mobility (μ_h) determined via the SCLC method from glass|ITO|PEDOT:PSS|HTM|MoO_3|Au devices. [h]Average HTM film conductivity (σ) obtained via a four-point measurement.

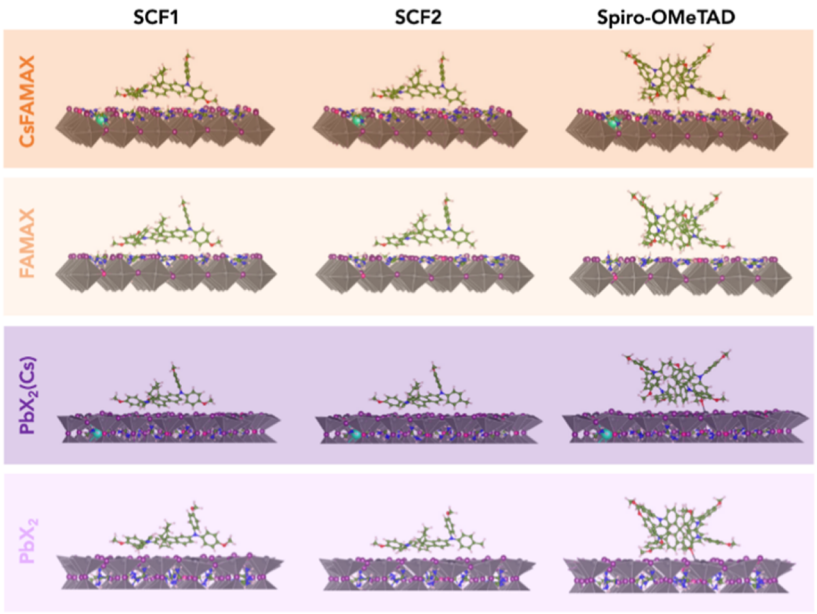

Figure 2. Lateral views of minimum-energy structure HTM/$Cs_{0.05}(FA_{0.83}MA_{0.17})_{0.95}Pb(I_{0.83}Br_{0.17})_3$ interfaces (HTM = **SCF1**, **SCF2**, and Spiro-OMeTAD) considering AX or PbX_2 terminations of the perovskite (010) surface with different compositions. AX-terminated surfaces with/without Cs are labeled CsFAMAX/FAMAX, while PbX_2-terminated surfaces with/without subsurface Cs are labeled PbX_2(Cs)/PbX_2. Color code: Pb (gray), I (violet), Cs (cyan), Br (pink), C (green), N (blue), O (red), and H (white).

The water contact angles (CAs) of the HTM films were measured from the same samples as PL and TRPL by using an Attension Theta Lite optical goniometer (Biolin Scientific AB, Sweden).

3. RESULTS AND DISCUSSION

The cost for the final products was evaluated at 29 and 33 €/g for **SCF1** and **SCF2**, respectively, significantly lower than what has been estimated for Spiro-OMeTAD (the raw material cost is 86 €/g).[20] Details on the cost analysis of the HTMs are given in the Supporting Information. The thermal, optical, and electrochemical properties of the **SCF**-HTMs are summarized in Table 1. The HTMs show a remarkable thermal stability (T_{dec} > 370 °C) and glass-transition temperatures (T_g > 80 °C) comparable to that of conventionally doped Spiro-OMeTAD (see Figure S11a,b in the Supporting Information).[21] Their HOMO energy levels are well aligned with the valence band (VB) maximum of the CsFAMA perovskite[22] and are similar to the HOMO levels of Spiro-OMeTAD (−5.02 eV) measured in the same electrochemical conditions (Figure S11d). The comparable absorption maxima and optical band gaps of **SCF1** and **SCF2** lead to LUMO energy values preluding to an efficient electron blocking from the conduction band of the perovskite active layer. The theoretical HOMO/LUMO energy values are consistent with those from the experimental electrochemical measurements, while the frontier orbitals display similar electronic distributions (Figure S12).

The hole mobility (μ_h) of SCF-HTMs and their conductivity (σ) are also presented in Table 1. **SCF1** displayed higher hole mobility and conductivity than those of **SCF2**, and their charge transport capabilities were compared to that of Spiro-OMeTAD HTM, both doped with and without *t*BP, Li-TFSI, and FK209 additives (as in traditional PSCs), under identical conditions. The hole mobilities obtained for both undoped and doped Spiro-OMeTAD (4.2×10^{-5} and 4.9×10^{-4} $cm^2\ V^{-1}\ s^{-1}$, respectively), as well as the conductivity of the undoped film (9.6×10^{-8} S cm^{-1}), are in good agreement with the reported values.[4,23−25] While **SCF1** and **SCF2** have a higher potential for effective charge transport than undoped Spiro-OMeTAD, doping raises the conductivity of Spiro-OMeTAD to a higher order of magnitude (with values typically reported in the 10^{-5} to 10^{-4} S cm^{-1} range).[26−28]

3.1. Theoretical Insights of the Perovskite|HTM Interface. We analyzed the interactions of our SCF-HTMs with the perovskite surface and compared them to those involving the Spiro-OMeTAD reference. While the interfacial behavior of Spiro-OMeTAD has been studied on different MAPI surfaces by a theoretical point of view,[29−33] no computational studies have explored the interface with the triple-cation perovskite so far. Here, we addressed all possible surface terminations of the triple-cation perovskite active layer for modeling the HTM/perovskite interactions. Both the large

https://doi.org/10.1021/acs.chemmater.3c00145
Chem. Mater. 2023, 35, 2975−2987

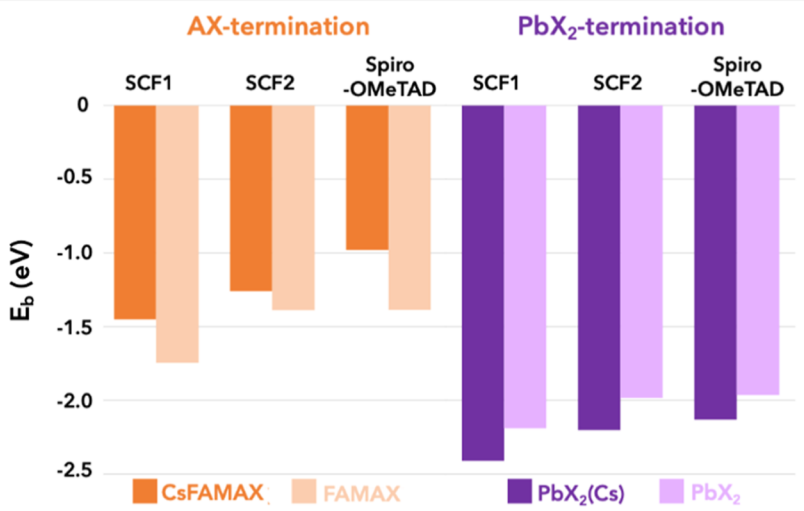

Figure 3. Computed binding energies of **SCF1**, **SCF2**, and Spiro-OMeTAD HTMs on the $Cs_{0.05}(FA_{0.83}MA_{0.17})_{0.95}Pb(I_{0.83}Br_{0.17})_3$ (010) surface for CsFAMAX (dark orange), FAMAX (light orange), PbX_2(Cs) (dark purple), and PbX_2 (purple)-terminated surfaces.

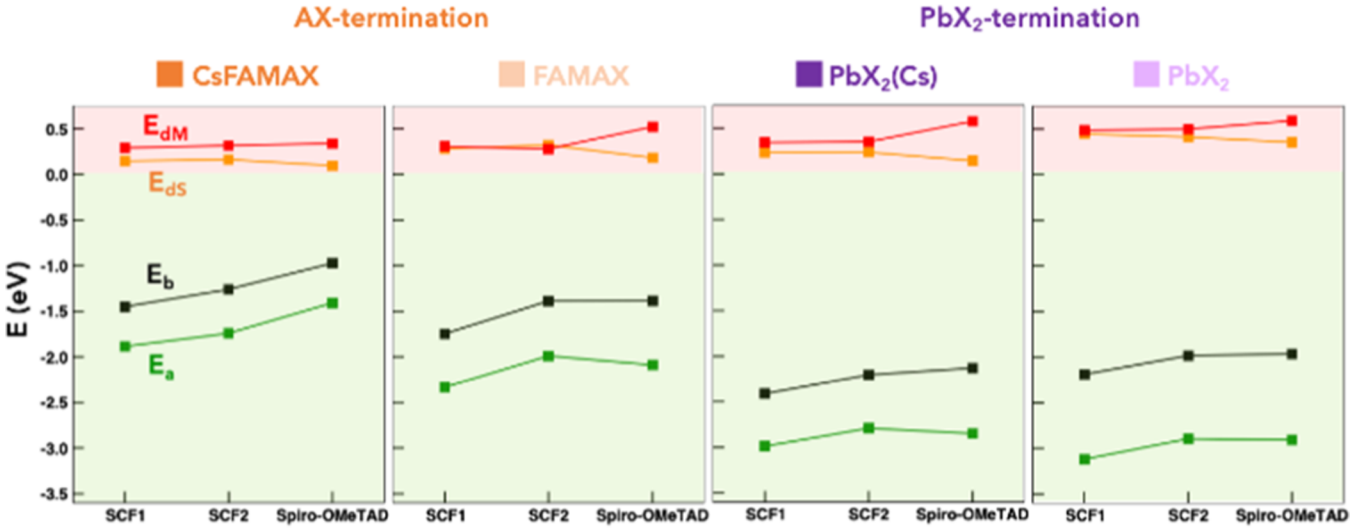

Figure 4. Decompositions of binding energies of HTMs **SCF1**, **SCF2**, and Spiro-OMeTAD on the $Cs_{0.05}(FA_{0.83}MA_{0.17})_{0.95}Pb(I_{0.83}Br_{0.17})_3$ (010) surface with AX or PbX_2 terminations with different compositions. AX-terminated surfaces with/without Cs are labeled CsFAMAX/FAMAX, while PbX_2-terminated surfaces with/without the subsurface Cs are labeled PbX_2(Cs)/PbX_2.

A cation halide (AX) and the lead halide (PbX_2) terminations of the $Cs_{0.05}(FA_{0.83}MA_{0.17})_{0.95}Pb(I_{0.83}Br_{0.17})_3$ perovskite (Figure S8) are depicted in Figure S9 (see the Supporting Information for further details on the structural model), and the optimized structures of the corresponding interfaces between the CsFAMA perovskite and **SCF1**, **SCF2**, and Spiro-OMeTAD HTM are shown in Figure 2.

An overview of the computed binding energies for these systems is collected in Figure 3. According to our calculations, **SCF1** forms the most stable interface with the perovskite for all terminations and surface compositions, with binding energies stronger up to 0.4 eV with respect to **SCF2** and Spiro-OMeTAD. Even if the latter two HTMs present similar binding energies, those of **SCF2** are slightly favorable over Spiro-OMeTAD. The enhanced interface realized with **SCF1** may promote the stability of the corresponding solar cells,[12] as will be demonstrated via stability studies.

Surface termination, i.e., whether the HTMs are adsorbed on the AX or PbX_2-type surface, has a more pronounced effect on binding energies than the different composition within a given termination. Binding energies drop ∼ 1 eV (from −1.45 to −2.41 eV in **SCF1**, from −1.26 to −2.20 eV in **SCF2**, and from −0.98 to −2.13 eV in Spiro-OMeTAD) when turning from the CsFAMAX termination to the PbX_2 (Cs) one. Different surface compositions have only a mild impact on binding energies (within the 0.17−0.4 eV range), with Cs stabilizing the HTM/PbX_2 interfaces but destabilizing the HTM/AX ones. Additionally, the SCF-HTMs present a more significant stabilization due to van der Waals forces than Spiro-OMETAD: Figure S15 shows the dispersion energy per atom (E_{vdW}/atom) contribution that dominates the HTM−perovskite binding. The contribution to the binding energies in terms of adhesion and distortion factors is displayed in Figure 4.

This analysis reveals that adhesion energy (E_a) is the dominant term for all studied HTMs, all of them having strong electronic interaction with the perovskite. E_a is more negative for **SCF1** on all terminations explored, while E_a(**SCF2**) and

https://doi.org/10.1021/acs.chemmater.3c00145
Chem. Mater. 2023, 35, 2975−2987

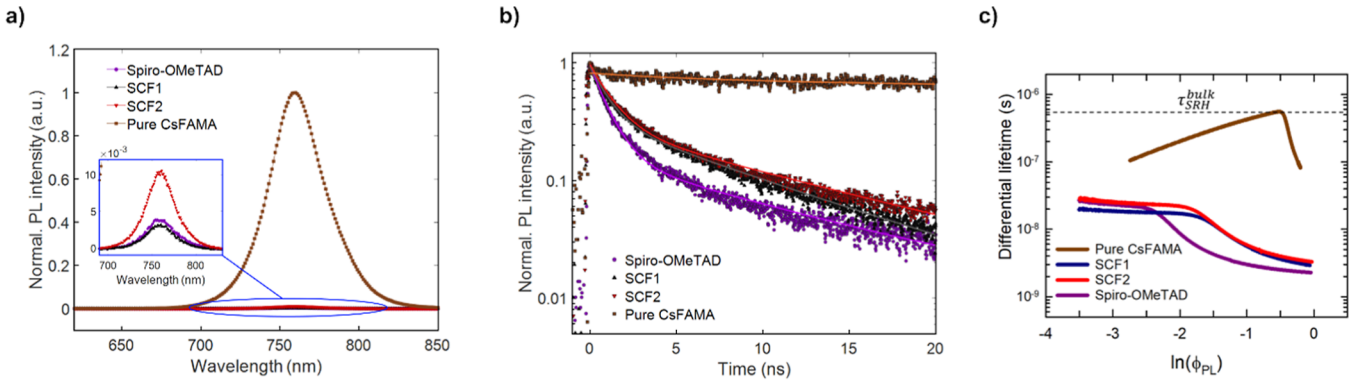

Figure 5. (a) Normalized PL spectra (excited at 600 nm) and (b) TRPL decays (excited at 405 nm with a time resolution of 60 ps and monitored at 755 nm) of glass/CsFAMA and glass/CsFAMA/HTM films with various HTMs including doped Spiro-OMeTAD as the reference. Solid lines show the fitting results with a rate law function. (c) Differential lifetime as a function of the logarithm of the PL intensity (ln ϕ_{PL}).

E_a(Spiro-OMeTAD) do not follow a particular trend (E_a(**SCF2**) < E_a(Spiro-OMeTAD) for CsFAMAX, E_a(**SCF2**) > E_a(Spiro-OMeTAD) for FAMAX and PbX_2(Cs), and E_a(**SCF2**) ∼ E_a(Spiro-OMeTAD) for PbX_2). Surface distortion energies (E_{dS}) are overall low, especially those induced by Spiro-OMeTAD. The key for the overall stabilization of **SCF1** and **SCF2** over Spiro-OMeTAD resides instead in the different molecular distortion patterns (E_{dM}). Spiro-OMeTAD presents a remarkably higher E_{dM} than **SCF1** and **SCF2** (up to ∼0.25 eV), which tips the scales toward the final E_b trend: E_b(**SCF1**) < E_b(**SCF2**) < E_b(Spiro-OMeTAD). This behavior could be ascribed to the presence of the orthogonal fragment in Spiro-OMETAD that enforces a molecular distortion in the surface anchoring, which is not achieved for the SCF-HTMs.

On the other hand, the structural analysis combined with the charge difference (CD) plot of HTM/perovskite interfaces allows us to explain the different stability of the SCF-HTMs. The molecule−surface distances (Figure S10) show that the functional groups $-OCH_3$ define the main interactions between all HTMs and surface termination. In general, the distances are overall lowest for **SCF1**. This result is confirmed by the CD plots in Figure S16, which shows a further interaction between the fluorene ring and the MA/FA cation in the **SCF1**−FAMAX interface. In conclusion, the most stable favorite binding energies of **SCF1** with respect to **SCF2** could be ascribed to the major number of $-OCH_3$ terminal-functional groups (adding further dispersion forces for anchoring to the perovskite surface) and a more favorable conformation that increases the SCF-HTM−perovskite interaction through the main fluorene moiety.

The electronic properties of the investigated HTM/perovskite interfaces have also been analyzed in terms of their projected density of states (pDOS). pDOS allow us to evaluate the energy difference of the HTM HOMO and the VB of the perovskite, which represents the thermodynamic driving force for hole extraction from the perovskite to the HTM. Defined this way, the HOMO of the HTM should be higher in energy than the perovskite's VB for an effective hole extraction. As can be seen in Figure S12, **SCF1**, **SCF2**, and Spiro-OMeTAD present a very similar electronic behavior for all terminations and compositions explored, with their HOMO well above the perovskite VB, in particular for the PbX_2 termination. Thus, **SCF1** and **SCF2** are not only predicted to form stable interfaces with $Cs_{0.05}(FA_{0.83}\ MA_{0.17})_{0.95}Pb(I_{0.83}Br_{0.17})_3$ but also to possess the required features for hole extraction.

3.2. Experimental Analysis of the Perovskite|HTM Interaction. The interaction between the CsFAMA perovskite and HTMs was analyzed by XPS using samples spin-coated with low concentration (0.25 mg mL^{-1} in chlorobenzene) of HTMs (Figures S17 and S18 and Table S1). Except for Cs, all the perovskite elements showed strong XPS signals before and after with the deposition of HTMs. The surface concentration of Cs was close to the detection limit, and the Cs-to-Pb atomic ratio at the surface was 0.003 (c.f., a nominal bulk ratio of 0.050), indicating strong surface depletion of Cs. Treatments with HTMs induced only little changes to the CsFAMA perovskite species but resulted in a clear and similar increase (from 0.4 to 1.6−1.8 at. %) in the O 1s signal at 532.7 eV (Figures S18a). This binding energy corresponds to C−O bonds at the surface and supports the modeled HTM interaction with CsFAMA via methoxy ($-OCH_3$) functional groups. Interaction via oxidation of metals (e.g., Pb−O[34]) can be excluded since metal oxides appear at binding energies <531 eV and where not detected.[35] On the other hand, unreacted methoxy groups ($-OCH_3$) have higher binding energies around 533.5 eV as measured for thicker layers of similar HTM materials.[34,36]

3.3. Hole Extraction Kinetics. The suitability of SCF-HTMs for hole extraction was confirmed via PL studies. Figure 5a compares the steady-state PL spectra of glass|CsFAMA and glass|CsFAMA|HTMs samples, including the doped Spiro-OMeTAD as the reference, both excited at 600 nm. A clear PL quenching was observed for all the HTMs. By comparing the PL amplitudes of pure perovskite and perovskite|HTM samples, the quenching efficiencies, i.e., hole extraction efficiency, were estimated to be 99.6, 99.7, and 99.1% for reference Spiro-OMeTAD, **SCF1**, and **SCF2**, respectively. This suggests that the HOMO levels of SCF-HTMs are aligned well with the VB of the CsFAMA perovskite, providing sufficient driving force for an efficient hole extraction reaction. The alignment of **SCF1** and **SCF2** is also supported by the computational results. We then assessed the hole extraction dynamics by measuring the TRPL decays for those same samples, as shown in Figure 5b. A gradual decay acceleration was monitored for glass|CsFAMA|SCF-HTMs when moving from **SCF2** to **SCF1**, revealing that the hole extraction process turns to be swifter, which is also in agreement with the PL quenching data.

To quantitatively analyze the PL decay data, a simple rate equation (see eq S3) was employed to fit the PL decays for the

https://doi.org/10.1021/acs.chemmater.3c00145
Chem. Mater. 2023, 35, 2975−2987

Table 2. Summarized Fitting Results of TRPL Decays for Various HTM-Coated Perovskite Films

HTM	k_1[a] (s^{-1})	k_2[b] ($s^{-1}cm^3$)	k_{HT}[c] (s^{-1})	ϕ_{ext}[d] (%)	surface recombination velocity (cm s^{-1})
Spiro-OMeTAD	1.1×10^7	3.5×10^{-10}	7.6×10^8	99.6	4.2×10^3
SCF1	2.7×10^7	3.3×10^{-10}	5.5×10^8	99.7	5.2×10^3
SCF2	3.1×10^7	3.4×10^{-10}	4.7×10^8	99.1	4.1×10^3

[a]First-order rate constants. [b]second-order rate constants. [c]Hole extraction rate constants. [d]Hole extraction efficiency.

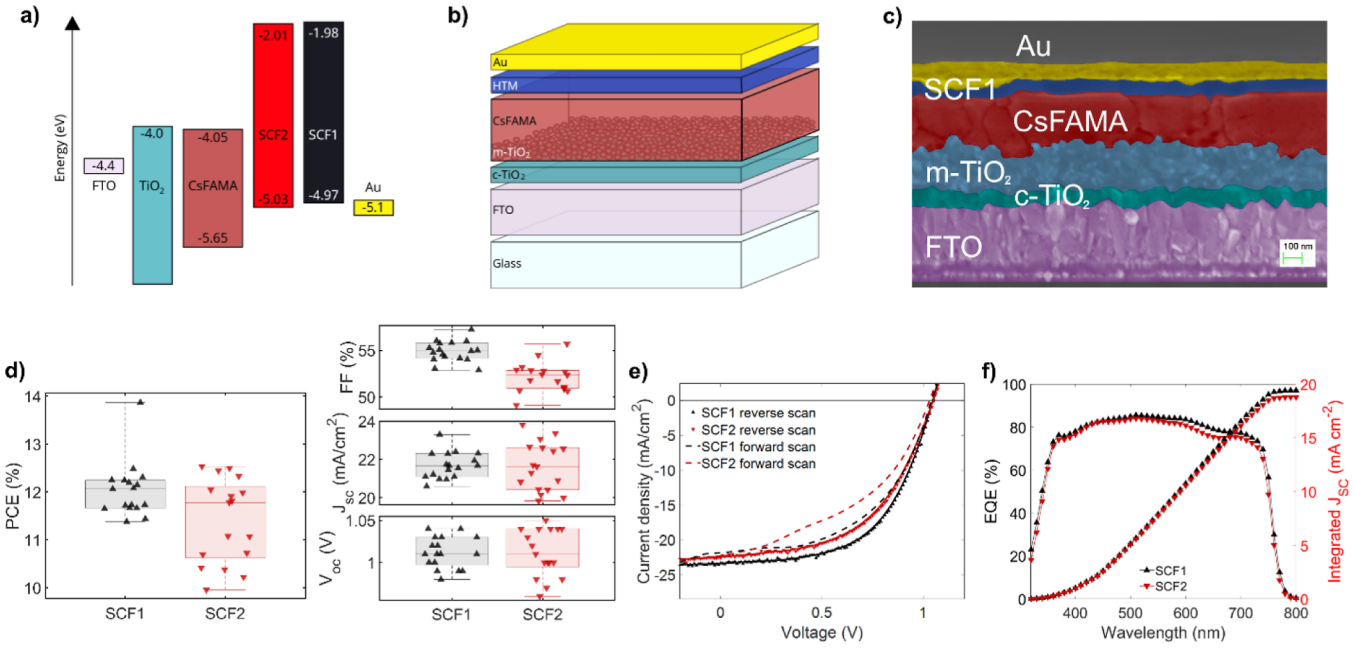

Figure 6. (a) Energy-level diagram for SCF-HTMs and other layers of the fabricated CsFAMA-PSCs. Aside from SCF-HTMs, the values have been taken from the literature.[39−41] (b) Structure of the fabricated mesoporous n−i−p solar cells. (c) Cross-sectional SEM image of a fabricated solar cell employing **SCF1** as the HTM. (d) Statistical representation of the photovoltaic parameters derived from the reverse scans of 17 PSCs for each SCF-HTM. Measurements were taken approximately 1 week after fabrication under 1 sun illumination (with a scan rate of 50 mV s^{-1}). (e) Current density (J)−voltage (V) curves of champion PSCs employing **SCF1** and **SCF2**. (f) External quantum efficiency (EQE) spectra and integrated J_{SC} values of typical SCF-HTM-based PSCs.

glass|CsFAMA|HTMs samples. These involve trap-assisted first-order recombination, non-geminate free charge carrier (electron and hole) second-order recombination, and interfacial hole extraction processes (see the detailed analysis method in the Supporting Information). The perovskite excited-state decay (glass|CsFAMA) was fitted with a simplified equation (see eq S5) containing only two components (first- and second-order recombination). The fitting results are presented as solid lines in Figure 5b, indicating that the rate law function can be used to fit the decay data for glass|CsFAMA|HTMs samples. Our global analysis confirms that the interfacial hole extraction process dominates. The extracted first-order (k_1), second-order (k_2), and hole extraction (k_{HT}) rate constants are summarized in Table 2.

We found that k_1 increases from 2.7×10^7 s^{-1} (**SCF1**) to 3.1×10^7 s^{-1} (**SCF2**), implying that **SCF1** indeed promotes the hindering of non-radiative recombination via traps compared to **SCF2**. This result is in agreement with the highest binding energy simulated for the perovskite|**SCF1** interface, which leads to the strong passivation of the perovskite surface. Accordingly, **SCF1** shows the largest hole extraction rate constant (k_{HT}) of 5.5×10^8 s^{-1}. It is noted that the second-order (k_2) rate constants for all the cases (including the reference Spiro-OMeTAD) are similar to each other, suggesting that the interfacial hole extraction reaction has a negligible effect on the non-geminate charge carrier recombination within the perovskite. Since the PL decays contain either two (glass|CsFAMA) or three (glass|CsFAMA|HTMs) components, we can describe the PL decays using the so-called differential lifetime, which has been recently utilized as one effective measure to qualify the charge-transfer dynamics at the interface between the perovskite and the charge acceptors.[37,38] The differential lifetime (τ_{PL}) can be calculated according to eq 6

$$\tau_{PL} = \left(-\frac{1}{m} \frac{d\ln(\phi_{PL})}{dt} \right)^{-1} \quad (6)$$

where $\phi_{PL}(t)$ is the PL intensity at t after the photoexcitation and m is a factor related to the injection level, which is set to 2 for the high-level injection (both types of charge carriers are present in approximately equal concentrations) in this work, by assuming a case of an intrinsic perovskite layer with negligible doping.[37] Figure 5c presents the plotting of the differential lifetime as a function of the logarithm of PL intensity, which allows extracting the effective Shockley Read Hall (SRH) lifetime in the bulk (glass/CsFAMA), namely, τ_{SRH}^{bulk} is 559.8 ns, in agreement with the earlier reported lifetime values for the CsFAMA perovskite.[38] Similarly, the effective SRH lifetimes in the process of hole extraction (glass|CsFAMA|HTMs), τ_{SRH}^{HTM}, can be also estimated to be 18.5 ns (**SCF1**), 23.4 ns (**SCF2**),

https://doi.org/10.1021/acs.chemmater.3c00145
Chem. Mater. 2023, 35, 2975−2987

Table 3. Averaged Photovoltaic Parameters, Hysteresis Index, and Resistance Values of 17 Solar Cells of Each HTM Characterized after Approximately 1 Week

HTM	PCE (%)	FF (%)	J_{sc} (mA cm^{-2})	V_{oc} (V)	H-index[a]	R_S[b] (Ω cm^2)	R_{SH}[c] (kΩ cm^2)
Spiro-OMeTAD	17.8 ± 1.0 (20.0)[d]	69.3 ± 1.9 (72.2)	22.5 ± 0.7 (23.5)	1.14 ± 0.03 (1.18)	1.05 ± 0.03 (1.06)	6.1 ± 0.8 (4.9)	1.82 ± 0.50 (1.89)
SCF1	12.0 ± 0.6 (13.9)	54.9 ± 1.1 (57.2)	21.7 ± 0.7 (23.3)	1.01 ± 0.02 (1.04)	1.10 ± 0.07 (1.16)	10.8 ± 0.6 (9.3)	0.55 ± 0.18 (0.61)
SCF2	11.4 ± 0.9 (12.7)	52.1 ± 1.5 (53.2)	21.6 ± 1.2 (22.5)	1.01 ± 0.03 (1.06)	1.08 ± 0.10 (1.25)	13.4 ± 1.3 (11.2)	0.45 ± 0.07 (0.44)

[a]Hysteresis index is calculated as PCE_{rev}/PCE_{for}, where "rev" and "for" stand for reverse and forward scans, respectively. [b]Series resistance. [c]Shunt resistance. [d]The photovoltaic figures of merit of the champion devices are reported in parentheses.

and 22.6 ns (Spiro-OMeTAD). Thus, it is possible to evaluate the surface recombination velocity at the various "perovskite|HTM" interfaces by employing the effective lifetime approach[37] according to eq 7

$$\tau_{SRH}^{HTM} = \left(\frac{1}{\tau_{SRH}^{bulk}} + \frac{S}{2d} \right)^{-1} \quad (7)$$

where $d \approx 500$ nm is the thickness of the CsFAMA perovskite layer, estimated from the cross-sectional scanning electron microscopy (SEM) study (see following section). The highest surface recombination velocity ($S = 5226.8$ cm s^{-1}) is obtained for the glass|CsFAMA|**SCF1** sample, while the reference sample containing Spiro-OMeTAD exhibits a slightly higher S (4246.1 cm s^{-1}) than that (4094.9 cm s^{-1}) of the **SCF2**-based sample (Table 2). The trend of S values is highly consistent with the PL quenching data, further confirming that the fastest hole extraction occurs at the perovskite|**SCF1** interface.

Using eq 5, the average hole trap densities (six devices per structure) were calculated: 2.47 × 10^{15} cm^{-3} (**SCF1**), 3.99 × 10^{15} cm^{-3} (**SCF2**), and 4.18 × 10^{15} cm^{-3} (Spiro-OMeTAD). This shows that **SCF1** can reduce the trap density compared to **SCF2** and Spiro-OMeTAD, consistent with the highest surface recombination velocity obtained for **SCF1** in the above analysis of TRPL decay dynamics. These results also suggest improved surface passivation thanks to better binding.

3.4. Performance of SCF-HTM-Based Solar Cells. Based on the electrochemical, computational, charge transport, and hole extraction studies, we developed PSCs with a conventional $n-i-p$ structure (glass|FTO|compact TiO_2|mesoporous TiO_2|CsFAMA|HTM|Au), in which the HTMs were employed without dopants. Figure 6a,b depicts the energy levels of the PSC constituents and the device architecture, respectively.

The optimized thickness of SCF-HTMs in PSCs (~90 nm) was obtained from a concentration of 10 mg mL^{-1} SCF-HTM in chlorobenzene (see Table S2 in the Supporting Information for the results with different concentrations of **SCF**-HTMs), as deduced by the cross-sectional SEM images of the fabricated solar cells reported in Figures 6c and S19. Further reducing the thickness of SCF layers led to decreased performance due to inadequate coverage of the perovskite layer. The reference HTM, i.e., doped Spiro-OMeTAD, has been found to perform best in PSCs at a thickness of approximately 200 nm.[42,43] The need to significantly reduce the thickness of SCF-HTMs for maximizing the performance in PSCs stems from the relatively low hole mobility and conductivity of SCF materials (vide supra) but leads to direct contact between the Au electrode and the perovskite (see Figure S19).

The performance of the solar cells was evaluated by recording $J-V$ characteristics both in the dark and under 1 sun illumination (AM 1.5G, 100 mW cm^{-2}). The PCE of SCF-HTM-based devices improved significantly after fabrication, with the most noticeable effect occurring within 1 week (see Section 2.5 for discussion). This spontaneous increase in the PCE of PSCs has been observed earlier and has been attributed to possible morphological,[44] photophysical, or doping[24,45,46] effects.

The averaged photovoltaic parameters from 17 devices are reported in Table 3 and their statistics are illustrated in Figure 6d. In addition to the devices based on SCF-HTMs, the performance of reference devices using doped Spiro-OMeTAD as the HTM (with otherwise identical structures) is also reported in Table 3 for comparison. Additionally, Figure 6e shows the comparison of the $J-V$ curves of the champion devices. The improved performance of **SCF1** over **SCF2** could be attributed to its greater hole mobility and hole extraction capability.

It should be noted that the photovoltaic data is based on devices with a 20 mm^2 area, which is significantly larger than the commonly reported ones for high-performance devices (≤10 mm^2).[47] Compared to the champion **SCF2** device (PCE 12.7%), the best **SCF1**-based PSC showed a higher PCE of 13.9%, with a significantly enhanced J_{SC} value of 23.3 mA cm^{-2} and an improved FF of 57.2%. The high J_{SC} is consistent with the efficient hole extraction from the VB of the perovskite to the HOMO level of **SCF1**, previously demonstrated by the PL quenching data and TRPL decay lifetimes. The **SCF1**-based PSCs also present a lower series resistance (R_S) than **SCF2** (see Table 2), with an average value of 11.2 Ω cm^2, indicating that the favorable contact between the perovskite and **SCF1** layers, as suggested by theoretical calculations (vide supra), can effectively hinder the charge recombination, hence resulting in a better FF. In addition, a clearly reduced hysteresis in the $J-V$ curve of the **SCF1**-based champion device (H-index = 1.16) is noted, ascribed to the fast hole transfer diffusing from the CsFAMA/**SCF1** interface right after the hole extraction, which thus reduces the built-in electric field at the interface.[48]

Despite the good current density of **SCF1**- and **SCF2**-based solar cells, their FF is distinctly lower than reference cells employing doped Spiro-OMeTAD. Decreased FFs, as well as higher R_S, are connected to lower hole mobility and conductivity, which appear to be the primary limiting factors for these SCF-based devices.[49] The doping of **SCF1** and **SCF2** was attempted using the same dopants as Spiro-OMeTAD, but the improvement was not sufficiently significant (Table S3).

Finally, we evaluated the EQE of fabricated SCF-based solar cells (i.e., before the self-doping effect). Both SCF-HTM-based PSCs reached an EQE peak up to ~85%, as illustrated in Figure 6f. The mismatch between the current density extracted from the $J-V$ characteristics and the EQE spectra lies within the acceptable range (10−20%) reported for PSCs.[50]

The charge carrier recombination pathways and limiting factors of the device performance were further analyzed by recording the $J-V$ characteristics of the PSCs under variable light intensity (between 0.1 and 1.2 suns). The variation of

https://doi.org/10.1021/acs.chemmater.3c00145
Chem. Mater. 2023, 35, 2975−2987

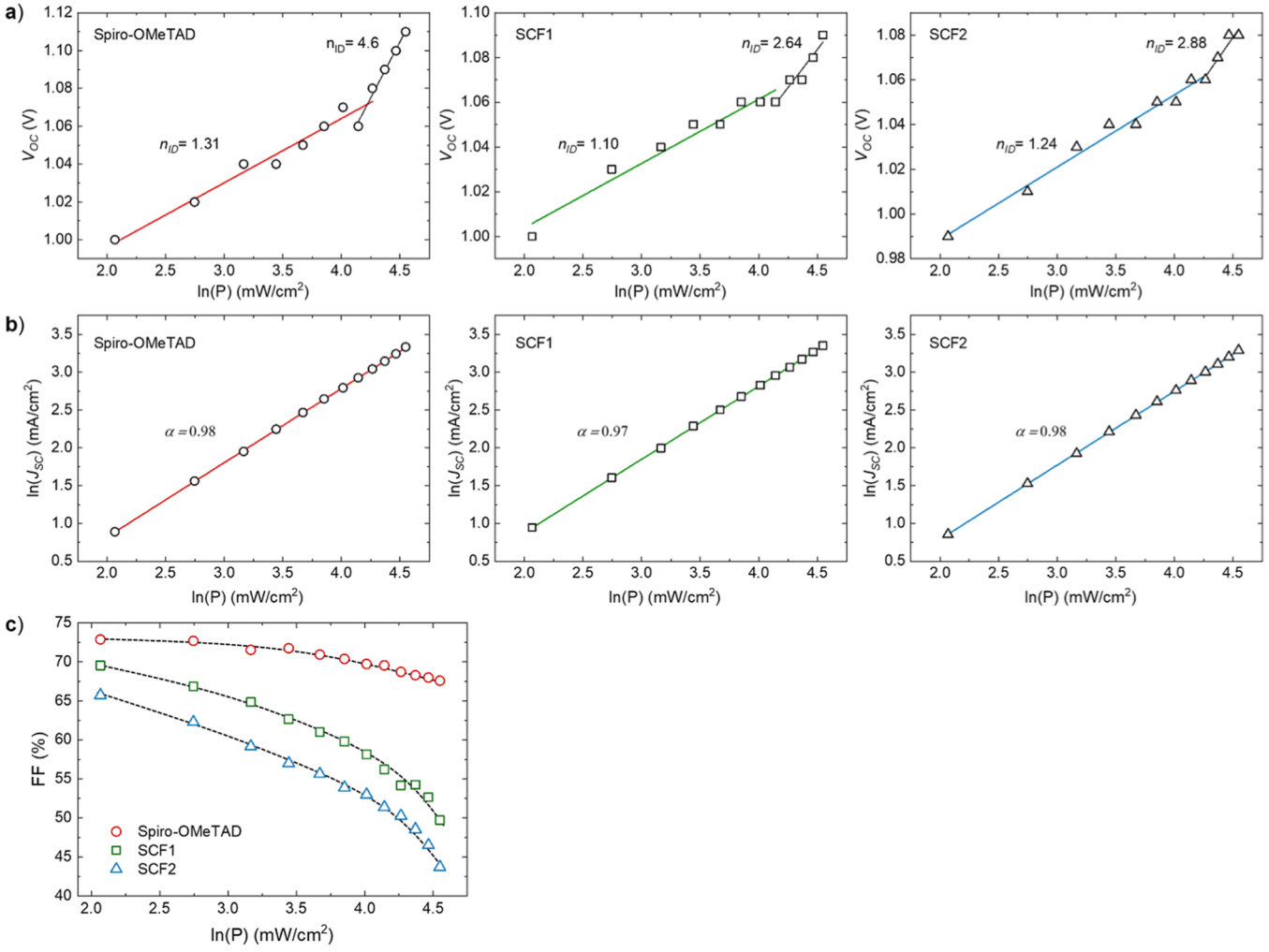

Figure 7. (a) Variation of V_{OC} *vs* light intensity (0.1−1.2 suns), (b) log−log plot of J_{SC} vs light intensity (0.1−1.2 suns), and (c) FF variation as a function of the illumination intensity for the three devices employing Spiro-OMeTAD, **SCF1**, and **SCF2** as the HTM.

V_{OC} as a function of the illumination intensity shows a slope of $n_{ID}k_BT/q$, where n_{ID} is the diode ideality factor and k_B, T, and q are Boltzmann's constant, temperature, and elementary charge, respectively. The majority of charge carriers recombine radiatively when n_{ID} = 1, whereas $n_{ID} \geq 2$ leads to SRH-type trap-assisted (non-radiative) recombination.[51] The V_{OC} variations of all the three devices (Figure 7a) show two linear segments with corresponding n_{ID} values of lower and higher than 2 under low- and high-intensity illuminations, respectively. It indicates increased trap-assisted recombination in the higher light intensity regime under open-circuit conditions.[14,52] The n_{ID} values in the low-intensity illumination were 1.31, 1.10, and 1.24 for the Spiro-OMeTAD-, **SCF1**-, and **SCF2**-based devices, respectively. The n_{ID} trend for the devices remains the same in the high-illumination regime also. Compared to the Spiro-OMeTAD-based device, the n_{ID} values are lower for those based on our HTMs. Notably, the **SCF1**-based device with the lowest n_{ID} value of 1.10 exhibits reduced trap-assisted recombination, which might be attributed to its better defect passivation capability. This result correlates well with the lower trap density as well as with the interfacial charge recombination dynamics observed for the **SCF1**-modified perovskite surface.

The power law dependence of J_{SC} on the light intensity ($J \propto P^{\alpha}$, where P is the light intensity and α is an exponential factor) can be obtained by a linear log−log plot of J_{SC} versus light intensity (Figure 7b). The exponent (α) values for all the three devices are close to unity (α = 0.97−0.98), which indicates that the number of bimolecular recombination is nearly the same for the three devices under the short-circuit conditions. This is reflected in similar J_{SC} values of the three devices. On the contrary, the dependence of FF on the illumination intensity for the three devices is quite different (Figure 7c). The FF slowly increases from 68 to 73% as the illumination changes from 1.0 to 0.1 suns in the case of the Spiro-OMeTAD-based device. In contrast, the other two devices witnessed a steep rise in the FF values. In detail, the FF of the **SCF2**-based device increases from 48 to 65% as the light intensity approaches 0.1 sun of intensity, while, in the case of the **SCF1**-based devices, it passes from 54 to 70%. The stronger inflection in FFs reaching 1.0 sun illumination evidenced for the **SCF1** and **SCF2** devices in comparison with the Spiro-OMeTAD-based cell is in agreement with their higher R_S, which are known to minimally impact the device performance at low light intensities.[53,54]

3.5. Stability Study. To assess the effect of SCF-HTMs on PSC stability, a long-term shelf lifetime evaluation was conducted together with a doped Spiro-OMeTAD reference cell. We remark the fact that we are comparing HTM layers (dopant-free SCF-HTMs and doped Spiro-OMeTAD) en-

https://doi.org/10.1021/acs.chemmater.3c00145
Chem. Mater. 2023, 35, 2975−2987

dowed with very similar glass-transition temperatures, thus ruling out the role of the film's thermal stability in interpreting the data on the long-term device performances. The stability experiments were carried out in air (40−50% relative humidity) on unencapsulated devices, which were stored in dry air (20−25% relative humidity) in darkness between the periodic measurements. The normalized PCEs of these samples over a period of 447 days are presented in Figure 8a. It becomes immediately apparent that the performance of

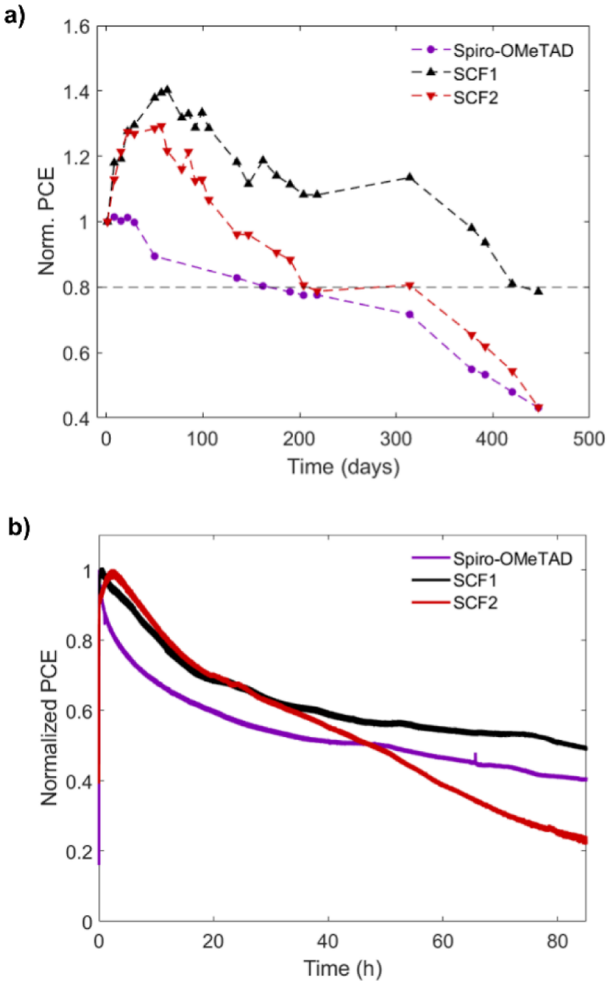

Figure 8. (a) Normalized PCEs of unencapsulated devices employing doped Spiro-OMeTAD and pristine SCF-HTMs observed over a period of 447 days. The T_{80} lifetimes of the various devices are indicated in the figure. The solar cells were stored in dry air ($T \approx 20$ °C, RH = 20−25%) under darkness. (b) Maximum power point (MPP) tracking curves of unencapsulated devices with Spiro-OMeTAD, **SCF1**, and **SCF2** under continuous 1 sun illumination.

SCF-HTM-based devices significantly improves for up to ≈60 days following their fabrication. This behavior was observed with all samples, and the effect was most noticeable over the course of 1 week after fabrication. The improvement was mostly tied to an increase in FF and V_{OC} (as can be seen in Figure S20 in the Supporting Information), indicating the possibility of an increase in the hole mobility of the SCF-HTMs.[38] It is hypothesized to be a form of self-doping, possibly due to reacting with oxygen, in a manner similar to Spiro-OMeTAD, although the period of improvement was much longer.[55] Doped Spiro-OMeTAD-based devices on the other simply degraded over time. As can be seen in Figure 8a, the reference cell (with Spiro-OMeTAD HTM) and the SCF2-based device degraded to 80% of their initial PCE after approximately 168 and 208 days of shelf storage, respectively, while the device employing **SCF1** has a T_{80} lifetime[56] of over 431 days, which is among the longest shelf lifetimes ever reported for all the types of PSCs. Compared to a previous study utilizing undoped Spiro-OMeTAD with a similar device structure,[38] the best case-projected T_{80} lifetime was 366 days, significantly less than that of our **SCF1** device (Figure S20a). In the literature, unencapsulated devices utilizing dopant-free HTMs degrade at different rates in air with the PCE degradation typically reported over a period shorter than 100 days.[57] Conversely, the devices based on our **SCF**-HTMs in the same time span (100 days) do not degrade, but their PCE is even still higher than the initial value. After 300 days, the PCEs of Spiro-OMeTAD- and **SCF1**-based PSCs became nearly identical, despite the big initial discrepancy between them (the PCE of the Spiro-OMeTAD cell in day 1 is more than double that of the **SCF1** cell). In other words, the excellent stability of SCF-HTMs, and especially of **SCF1**, compensates their inability of leading to top-efficiency PSCs because of the modest intrinsic properties (i.e., hole mobility and conductivity). This highlights the importance of looking at the efficiency and stability as a whole[58] when evaluating a device, in this case for the selection of an HTM, especially if other important advantages are gained, like the facile synthesis of the material.

The significant shelf stability of SCF-HTMs suggests that they can effectively cover the perovskite. This is also supported by theoretical calculations (vide supra), where the lower SCF-HTM distortion energies (E_{dM}) favor the adhesion on perovskite surfaces, allowing them to form a protective barrier that slows down the penetration of moisture. The study of the water CA confirms a clear difference in hydrophobicity between SCF-HTMs and (doped and undoped) Spiro-OMeTAD, as shown in Figure S21 in the Supporting Information. The highest CAs are for SCF-HTMs and for undoped Spiro-OMeTAD, which were expected as doping with hygroscopic Li-TFSI and *t*BP is known to increase the hydrophilicity of Spiro-OMeTAD films.[59,60] Based on these results, the SCF films can be considered quite hydrophobic, which is one factor explaining the longer shelf lifetime of devices employing them, as perovskites are vulnerable to moisture. Therefore, the differences in the long-term stability expressed by SCF-HTM devices can be rationalized by the slower perovskite degradation promoted by water in comparison with doped Spiro-OMeTAD behavior and the improved interface between the perovskite and SCF-HTMs highlighted by the simulation study.

Additionally, the stability of unencapsulated devices employing Spiro-OMeTAD, **SCF1**, and **SCF2** was also monitored under 1 sun constant illumination for 85 h in MPP conditions. The MPP tracking curves of the three samples are reported in Figure 8b. The **SCF1**-based device exhibits the highest stability compared to either **SCF2**-based or reference-doped Spiro-OMeTAD devices, further confirming the advantages of this HTM. The main reason of the stable performance of **SCF1** lies most likely in its capability of effectively passivating the CsFAMA/**SCF1** interface,[48,61] as supported by the findings of our computational study.

https://doi.org/10.1021/acs.chemmater.3c00145
Chem. Mater. 2023, 35, 2975−2987

4. CONCLUSIONS

In summary, we have designed and synthesized dopant-free fluorene-based HTMs (**SCF1** and **SCF2**) derived from the well-known Spiro-OMeTAD, which can form a stable interface with the triple-cation CsFAMA perovskite. Our simulations show that a key factor in the enhanced binding energies of **SCF2** and especially **SCF1** is their reduced molecular distortion over the more complex Spiro-OMeTAD. At the same time, both SCF-HTMs present significantly lower material and fabrication cost. The enhanced perovskite|**SCF1** interface is reflected in excellent hole extraction, low hole trap density, and an impressive shelf lifetime (T_{80} = 431 days) of the corresponding unencapsulated devices, which is over twice as long as that of Spiro-OMeTAD and **SCF2** devices and one of the longest lifetimes ever reported for PSCs. Our work highlights the need to specifically match the perovskite and HTMs in order to attain stable PSCs via effective chemical bonding.

■ ASSOCIATED CONTENT

Supporting Information

The Supporting Information is available free of charge at https://pubs.acs.org/doi/10.1021/acs.chemmater.3c00145.

Details on material synthesis and characterization, cost analysis, computational study, as well as additional figures and supplementary results (PDF)

■ AUTHOR INFORMATION

Corresponding Authors

Roberto Grisorio − *Dipartimento di Ingegneria Civile, Ambientale, del Territorio, Edile e di Chimica (DICATECh), Politecnico di Bari, Bari 70125, Italy; CNR NANOTEC—Istituto di Nanotecnologia, Lecce 73100, Italy;* orcid.org/0000-0002-3698-9370; Email: Roberto.grisorio@poliba.it

Paola Vivo − *Hybrid Solar Cells, Faculty of Engineering and Natural Sciences, Tampere University, Tampere FI-33014, Finland;* orcid.org/0000-0003-2872-6922; Email: paola.vivo@tuni.fi

Authors

Paavo Mäkinen − *Hybrid Solar Cells, Faculty of Engineering and Natural Sciences, Tampere University, Tampere FI-33014, Finland*

Francesca Fasulo − *Department of Chemical Sciences, University of Naples Federico II, Naples 80126, Italy*

Maning Liu − *Hybrid Solar Cells, Faculty of Engineering and Natural Sciences, Tampere University, Tampere FI-33014, Finland;* orcid.org/0000-0001-9875-0966

G. Krishnamurthy Grandhi − *Hybrid Solar Cells, Faculty of Engineering and Natural Sciences, Tampere University, Tampere FI-33014, Finland;* orcid.org/0000-0001-9986-1000

Daniele Conelli − *Dipartimento di Ingegneria Civile, Ambientale, del Territorio, Edile e di Chimica (DICATECh), Politecnico di Bari, Bari 70125, Italy*

Basheer Al-Anesi − *Hybrid Solar Cells, Faculty of Engineering and Natural Sciences, Tampere University, Tampere FI-33014, Finland;* orcid.org/0000-0001-8347-9309

Harri Ali-Löytty − *Surface Science Group, Photonics Laboratory, Tampere University, Tampere FI-33014, Finland;* orcid.org/0000-0001-8746-7268

Kimmo Lahtonen − *Faculty of Engineering and Natural Sciences, Tampere University, Tampere FI-33014, Finland;* orcid.org/0000-0002-8138-7918

Sami Toikkonen − *Hybrid Solar Cells, Faculty of Engineering and Natural Sciences, Tampere University, Tampere FI-33014, Finland*

Gian Paolo Suranna − *Dipartimento di Ingegneria Civile, Ambientale, del Territorio, Edile e di Chimica (DICATECh), Politecnico di Bari, Bari 70125, Italy; CNR NANOTEC—Istituto di Nanotecnologia, Lecce 73100, Italy*

Ana Belén Muñoz-García − *Department of Physics "Ettore Pancini", University of Naples Federico II, Naples 80126, Italy;* orcid.org/0000-0002-9940-7358

Michele Pavone − *Department of Chemical Sciences, University of Naples Federico II, Naples 80126, Italy*

Complete contact information is available at: https://pubs.acs.org/10.1021/acs.chemmater.3c00145

Author Contributions

The manuscript was written through contributions of all authors. All authors have given approval to the final version of the manuscript.

Notes

The authors declare no competing financial interest.

■ ACKNOWLEDGMENTS

Dr. Maria Rosaria Taurino (Agro.Biolab Laboratory s.r.l.) is gratefully acknowledged for carrying out ESI-MS analysis. P.V. thanks the financial support of Jane and Aatos Erkko foundation (SOL-TECH project). M.L. acknowledges the Finnish Cultural Foundation (no. 00220107) for funding. This work was part of the Academy of Finland Flagship Programme, Photonics Research and Innovation (PREIN), Decision no. 320165. R.G. acknowledges the Apulia Region for the NANO-3D project (cod: 55FF6B6F). The computing resources and the related technical support used for this work have been provided by CRESCO/ENEA-GRID High Performance Computing infrastructure and its staff. CRESCO/ENEAGRID High Performance Computing infrastructure is funded by ENEA, Italy, the Italian National Agency for New Technologies, Energy and Sustainable Economic Development and by Italian and European research programs; see https://www.cresco.enea.it for information.

■ REFERENCES

(1) Best Research-Cell. Efficiency Chart|Photovoltaic Research| NREL. https://www.nrel.gov/pv/cell-efficiency.html (accessed Feb 21, 2022).

(2) Shao, S.; Loi, M. A. The Role of the Interfaces in Perovskite Solar Cells. *Adv. Mater. Interfaces* **2020**, *7*, 1901469.

(3) Schulz, P.; Cahen, D.; Kahn, A. Halide Perovskites: Is It All about the Interfaces? *Chem. Rev.* **2019**, *119*, 3349−3417.

(4) Park, N.-G.; Grätzel, M.; Miyasaka, T.; Zhu, K.; Emery, K. Towards Stable and Commercially Available Perovskite Solar Cells. *Nat. Energy* **2016**, *1*, 16152.

(5) Correa-Baena, J.-P.; Saliba, M.; Buonassisi, T.; Grätzel, M.; Abate, A.; Tress, W.; Hagfeldt, A. Promises and Challenges of Perovskite Solar Cells. *Sci.* **2017**, *358*, 739−744.

(6) Vivo, P.; Salunke, J.; Priimagi, A. Hole-Transporting Materials for Printable Perovskite Solar Cells. *Materials* **2017**, *10*, 1087.

(7) Yin, X.; Song, Z.; Li, Z.; Tang, W. Toward Ideal Hole Transport Materials: A Review on Recent Progress in Dopant-Free Hole Transport Materials for Fabricating Efficient and Stable Perovskite Solar Cells. *Energy Environ. Sci.* **2020**, *13*, 4057−4086.

(8) Ding, X.; Wang, H.; Chen, C.; Li, H.; Tian, Y.; Li, Q.; Wu, C.; Ding, L.; Yang, X.; Cheng, M. Passivation functionalized phenothiazine-based hole transport material for highly efficient perovskite solar cell with efficiency exceeding 22%. *Chem. Eng. J.* **2021**, *410*, 128328.
(9) Zhao, B. X.; Yao, C.; Gu, K.; Liu, T.; Xia, Y.; Loo, Y.-L. A Hole-Transport Material That Also Passivates Perovskite Surface Defects for Solar Cells with Improved Efficiency and Stability. *Energy Environ. Sci.* **2020**, *13*, 4334−4343.
(10) Wang, S.-Y.; Chen, C.-P.; Chung, C.-L.; Hsu, C.-W.; Hsu, H.-L.; Wu, T.-H.; Zhuang, J.-Y.; Chang, C.-J.; Chen, H. M.; Chang, Y. J. Defect Passivation by Amide-Based Hole-Transporting Interfacial Layer Enhanced Perovskite Grain Growth for Efficient p-i-n Perovskite Solar Cells. *ACS Appl. Mater. Interfaces* **2019**, *11*, 40050−40061.
(11) Zhang, J.; Guo, S.; Zhu, M.; Li, C.; Chen, J.; Liu, L.; Xiang, S.; Zhang, Z. Simultaneous Defect Passivation and Hole Mobility Enhancement of Perovskite Solar Cells by Incorporating Anionic Metal-Organic Framework into Hole Transport Materials. *Chem. Eng. J.* **2021**, *408*, 127328.
(12) Canil, L.; Salunke, J.; Wang, Q.; Liu, M.; Köbler, H.; Flatken, M.; Gregori, L.; Meggiolaro, D.; Ricciarelli, D.; De Angelis, F.; Stolterfoht, M.; Neher, D.; Priimagi, A.; Vivo, P.; Abate, A. Halogen-Bonded Hole-Transport Material Suppresses Charge Recombination and Enhances Stability of Perovskite Solar Cells. *Adv. Energy Mater.* **2021**, *11*, 2101553.
(13) Wang, C.; Liu, M.; Rahman, S.; Pasanen, H. P.; Tian, J.; Li, J.; Deng, Z.; Zhang, H.; Vivo, P. Hydrogen Bonding Drives the Self-Assembling of Carbazole-Based Hole-Transport Material for Enhanced Efficiency and Stability of Perovskite Solar Cells. *Nano Energy* **2022**, *101*, 107604.
(14) Ryu, S.; Nguyen, D. C.; Ha, N. Y.; Park, H. J.; Ahn, Y. H.; Park, J.-Y.; Lee, S. Light Intensity-Dependent Variation in Defect Contributions to Charge Transport and Recombination in a Planar MAPbI3 Perovskite Solar Cell. *Sci. Rep.* **2019**, *9*, 19846.
(15) Grisorio, R.; Roose, B.; Colella, S.; Listorti, A.; Suranna, G. P.; Abate, A. Molecular Tailoring of Phenothiazine-Based Hole-Transporting Materials for High-Performing Perovskite Solar Cells. *ACS Energy Lett.* **2017**, *2*, 1029−1034.
(16) Grisorio, R.; Iacobellis, R.; Listorti, A.; De Marco, L.; Cipolla, M. P.; Manca, M.; Rizzo, A.; Abate, A.; Gigli, G.; Suranna, G. P. Rational Design of Molecular Hole-Transporting Materials for Perovskite Solar Cells: Direct versus Inverted Device Configurations. *ACS Appl. Mater. Interfaces* **2017**, *9*, 24778−24787.
(17) Fairley, N.; Fernandez, V.; Richard-Plouet, M.; Guillot-Deudon, C.; Walton, J.; Smith, E.; Flahaut, D.; Greiner, M.; Biesinger, M.; Tougaard, S.; Morgan, D.; Baltrusaitis, J. Systematic and Collaborative Approach to Problem Solving Using X-Ray Photoelectron Spectroscopy. *Appl. Surf. Sci. Adv.* **2021**, *5*, 100112.
(18) Wang, Y.; Djurišić, A. B.; Chen, W.; Liu, F.; Cheng, R.; Ping Feng, S.; Ng, A. M. C.; He, Z. Metal oxide charge transport layers in perovskite solar cells-optimising low temperature processing and improving the interfaces towards low temperature processed, efficient and stable devices. *J. Phys. Energy* **2020**, *3*, 012004.
(19) Li, W.; Lai, X.; Meng, F.; Li, G.; Wang, K.; Kyaw, A. K. K.; Sun, X. W. Efficient Defect-Passivation and Charge-Transfer with Interfacial Organophosphorus Ligand Modification for Enhanced Performance of Perovskite Solar Cells. *Sol. Energy Mater. Sol. Cells* **2020**, *211*, 110527.
(20) Petrus, M. L.; Bein, T.; Dingemans, T. J.; Docampo, P. A Low Cost Azomethine-Based Hole Transporting Material for Perovskite Photovoltaics. *J. Mater. Chem. A* **2015**, *3*, 12159−12162.
(21) Malinauskas, T.; Tomkute-Luksiene, D.; Sens, R.; Daskeviciene, M.; Send, R.; Wonneberger, H.; Jankauskas, V.; Bruder, I.; Getautis, V. Enhancing Thermal Stability and Lifetime of Solid-State Dye-Sensitized Solar Cells via Molecular Engineering of the Hole-Transporting Material Spiro-OMeTAD. *ACS Appl. Mater. Interfaces* **2015**, *7*, 11107−11116.
(22) Zhang, H.; Liu, M.; Yang, W.; Judin, L.; Hukka, T. I.; Priimagi, A.; Deng, Z.; Vivo, P. Thionation Enhances the Performance of Polymeric Dopant-Free Hole-Transporting Materials for Perovskite Solar Cells. *Adv. Mater. Interfaces* **2019**, *6*, 1901036.
(23) Pham, N. D.; Shang, J.; Yang, Y.; Hoang, M. T.; Tiong, V. T.; Wang, X.; Fan, L.; Chen, P.; Kou, L.; Wang, L.; Wang, H. Alkaline-Earth Bis(Trifluoromethanesulfonimide) Additives for Efficient and Stable Perovskite Solar Cells. *Nano Energy* **2020**, *69*, 104412.
(24) Ngo, T. T.; Barea, E. M.; Tena-Zaera, R.; Mora-Seró, I. Spray-Pyrolyzed ZnO as Electron Selective Contact for Long-Term Stable Planar CH3NH3PbI3 Perovskite Solar Cells. *ACS Appl. Energy Mater.* **2018**, *1*, 4057−4064.
(25) Abate, A.; Leijtens, T.; Pathak, S.; Teuscher, J.; Avolio, R.; Errico, M. E.; Kirkpatrik, J.; Ball, J. M.; Docampo, P.; McPherson, I.; Snaith, H. J. Lithium salts as "redox active" p-type dopants for organic semiconductors and their impact in solid-state dye-sensitized solar cells. *Phys. Chem. Chem. Phys.* **2013**, *15*, 2572.
(26) Tabor, D. P.; Chiykowski, V. A.; Friederich, P.; Cao, Y.; Dvorak, D. J.; Berlinguette, C. P.; Aspuru-Guzik, A. Design Rules for High Mobility Xanthene-Based Hole Transport Materials. *Chem. Sci.* **2019**, *10*, 8360−8366.
(27) Petrus, M. L.; Music, A.; Closs, A. C.; Bijleveld, J. C.; Sirtl, M. T.; Hu, Y.; Dingemans, T. J.; Bein, T.; Docampo, P. Design Rules for the Preparation of Low-Cost Hole Transporting Materials for Perovskite Solar Cells with Moisture Barrier Properties. *J. Mater. Chem. A* **2017**, *5*, 25200−25210.
(28) Xu, B.; Bi, D.; Hua, Y.; Liu, P.; Cheng, M.; Grätzel, M.; Kloo, L.; Hagfeldt, A.; Sun, L. A low-cost spiro[fluorene-9,9′-xanthene]-based hole transport material for highly efficient solid-state dye-sensitized solar cells and perovskite solar cells. *Energy Environ. Sci.* **2016**, *9*, 873−877.
(29) Coppola, C.; Pecoraro, A.; Muñoz-García, A. B.; Infantino, R.; Dessì, A.; Reginato, G.; Basosi, R.; Sinicropi, A.; Pavone, M. Electronic Structure and Interfacial Features of Triphenylamine- and Phenothiazine-Based Hole Transport Materials for Methylammonium Lead Iodide Perovskite Solar Cells. *Phys. Chem. Chem. Phys.* **2022**, *24*, 14993−15002.
(30) Saliba, M.; Orlandi, S.; Matsui, T.; Aghazada, S.; Cavazzini, M.; Correa-Baena, J.-P.; Gao, P.; Scopelliti, R.; Mosconi, E.; Dahmen, K.-H.; De Angelis, F.; Abate, A.; Hagfeldt, A.; Pozzi, G.; Graetzel, M.; Nazeeruddin, M. K. A Molecularly Engineered Hole-Transporting Material for Efficient Perovskite Solar Cells. *Nat. Energy* **2016**, *1*, 15017.
(31) Torres, A.; Rego, L. G. C. Surface Effects and Adsorption of Methoxy Anchors on Hybrid Lead Iodide Perovskites: Insights for Spiro-MeOTAD Attachment. *J. Phys. Chem. C* **2014**, *118*, 26947−26954.
(32) Yin, J.; Cortecchia, D.; Krishna, A.; Chen, S.; Mathews, N.; Grimsdale, A. C.; Soci, C. Interfacial Charge Transfer Anisotropy in Polycrystalline Lead Iodide Perovskite Films. *J. Phys. Chem. Lett.* **2015**, *6*, 1396−1402.
(33) Wang, Q.; Mosconi, E.; Wolff, C.; Li, J.; Neher, D.; De Angelis, F.; Suranna, G. P.; Grisorio, R.; Abate, A. Rationalizing the Molecular Design of Hole-Selective Contacts to Improve Charge Extraction in Perovskite Solar Cells. *Adv. Energy Mater.* **2019**, *9*, 1900990.
(34) Cai, N.; Li, F.; Chen, Y.; Luo, R.; Hu, T.; Lin, F.; Yiu, S.; Liu, D.; Lei, D.; Zhu, Z.; Jen, A. K. Y. Synergistical Dipole-Dipole Interaction Induced Self-Assembly of Phenoxazine-Based Hole-Transporting Materials for Efficient and Stable Inverted Perovskite Solar Cells. *Angew. Chem. Int. Ed.* **2021**, *60*, 20437−20442.
(35) Naumkin, A. V.; Kraut-Vass, A.; Gaarenstroom, S. W.; Powell, C. J. *NIST X-Ray Photoelectron Spectroscopy Database, NIST Standard Reference Database Number 20*; National Institute of Standards and Technology: Gaithersburg MD, 2008; p 20899.
(36) Wang, Y.; Liao, Q.; Chen, J.; Huang, W.; Zhuang, X.; Tang, Y.; Li, B.; Yao, X.; Feng, X.; Zhang, X.; Su, M.; He, Z.; Marks, T. J.; Facchetti, A.; Guo, X. Teaching an Old Anchoring Group New Tricks: Enabling Low-Cost, Eco-Friendly Hole-Transporting Materials for Efficient and Stable Perovskite Solar Cells. *J. Am. Chem. Soc.* **2020**, *142*, 16632−16643.

https://doi.org/10.1021/acs.chemmater.3c00145
Chem. Mater. 2023, 35, 2975−2987

(37) Krückemeier, L.; Krogmeier, B.; Liu, Z.; Rau, U.; Kirchartz, T. Understanding Transient Photoluminescence in Halide Perovskite Layer Stacks and Solar Cells. *Adv. Energy Mater.* **2021**, *11*, 2003489.
(38) Liu, M.; Dahlström, S.; Ahläng, C.; Wilken, S.; Degterev, A.; Matuhina, A.; Hadadian, M.; Markkanen, M.; Aitola, K.; Kamppinen, A.; Deska, J.; Mangs, O.; Nyman, M.; Lund, P. D.; Smått, J.-H.; Österbacka, R.; Vivo, P. Beyond Hydrophobicity: How F4-TCNQ Doping of the Hole Transport Material Improves Stability of Mesoporous Triple-Cation Perovskite Solar Cells. *J. Mater. Chem. A* **2022**, *10*, 11721−11731.
(39) Kim, H.-S.; Lee, C.-R.; Im, J.-H.; Lee, K.-B.; Moehl, T.; Marchioro, A.; Moon, S.-J.; Humphry-Baker, R.; Yum, J.-H.; Moser, J. E.; Grätzel, M.; Park, N.-G. Lead Iodide Perovskite Sensitized All-Solid-State Submicron Thin Film Mesoscopic Solar Cell with Efficiency Exceeding 9%. *Sci. Rep.* **2012**, *2*, 591.
(40) Piatkowski, P.; Cohen, B.; Javier Ramos, F.; Di Nunzio, M.; Nazeeruddin, M. K.; Grätzel, M.; Ahmad, S.; Douhal, A. Direct Monitoring of Ultrafast Electron and Hole Dynamics in Perovskite Solar Cells. *Phys. Chem. Chem. Phys.* **2015**, *17*, 14674−14684.
(41) Makuta, S.; Liu, M.; Endo, M.; Nishimura, H.; Wakamiya, A.; Tachibana, Y. Photo-excitation intensity dependent electron and hole injections from lead iodide perovskite to nanocrystalline TiO2 and spiro-OMeTAD. *Chem. Commun.* **2016**, *52*, 673−676.
(42) Kim, G.-W.; Shinde, D. V.; Park, T. Thickness of the Hole Transport Layer in Perovskite Solar Cells: Performance versus Reproducibility. *RSC Adv.* **2015**, *5*, 99356−99360.
(43) Marinova, N.; Tress, W.; Humphry-Baker, R.; Dar, M. I.; Bojinov, V.; Zakeeruddin, S. M.; Nazeeruddin, M. K.; Grätzel, M. Light Harvesting and Charge Recombination in CH3NH3PbI3 Perovskite Solar Cells Studied by Hole Transport Layer Thickness Variation. *ACS Nano* **2015**, *9*, 4200−4209.
(44) Roose, B.; Ummadisingu, A.; Correa-Baena, J.-P.; Saliba, M.; Hagfeldt, A.; Graetzel, M.; Steiner, U.; Abate, A. Spontaneous Crystal Coalescence Enables Highly Efficient Perovskite Solar Cells. *Nano Energy* **2017**, *39*, 24−29.
(45) Ito, N.; Kamarudin, M. A.; Hirotani, D.; Zhang, Y.; Shen, Q.; Ogomi, Y.; Iikubo, S.; Minemoto, T.; Yoshino, K.; Hayase, S. Mixed Sn-Ge Perovskite for Enhanced Perovskite Solar Cell Performance in Air. *J. Phys. Chem. Lett.* **2018**, *9*, 1682−1688.
(46) Bi, C.; Zheng, X.; Chen, B.; Wei, H.; Huang, J. Spontaneous Passivation of Hybrid Perovskite by Sodium Ions from Glass Substrates: Mysterious Enhancement of Device Efficiency Revealed. *ACS Energy Lett.* **2017**, *2*, 1400−1406.
(47) Lu, J.; Lin, X.; Jiao, X.; Gengenbach, T.; Scully, A. D.; Jiang, L.; Tan, B.; Sun, J.; Li, B.; Pai, N.; Bach, U.; Simonov, A. N.; Cheng, Y.-B. Interfacial Benzenethiol Modification Facilitates Charge Transfer and Improves Stability of Cm-Sized Metal Halide Perovskite Solar Cells with up to 20% Efficiency. *Energy Environ. Sci.* **2018**, *11*, 1880−1889.
(48) Li, R.; Liu, M.; Matta, S. K.; Hiltunen, A.; Deng, Z.; Wang, C.; Dai, Z.; Russo, S. P.; Vivo, P.; Zhang, H. Sulfonated Dopant-Free Hole-Transport Material Promotes Interfacial Charge Transfer Dynamics for Highly Stable Perovskite Solar Cells. *Adv. Sustain. Syst.* **2021**, *5*, 2100244.
(49) Le Corre, V. M.; Stolterfoht, M.; Perdigón Toro, L.; Feuerstein, M.; Wolff, C.; Gil-Escrig, L.; Bolink, H. J.; Neher, D.; Koster, L. J. A. Charge Transport Layers Limiting the Efficiency of Perovskite Solar Cells: How To Optimize Conductivity, Doping, and Thickness. *ACS Appl. Energy Mater.* **2019**, *2*, 6280−6287.
(50) Saliba, M.; Etgar, L. Current Density Mismatch in Perovskite Solar Cells. *ACS Energy Lett.* **2020**, *5*, 2886−2888.
(51) Tress, W.; Yavari, M.; Domanski, K.; Yadav, P.; Niesen, B.; Correa Baena, J. P.; Hagfeldt, A.; Graetzel, M. Interpretation and Evolution of Open-Circuit Voltage, Recombination, Ideality Factor and Subgap Defect States during Reversible Light-Soaking and Irreversible Degradation of Perovskite Solar Cells. *Energy Environ. Sci.* **2018**, *11*, 151−165.
(52) Ryu, S.; Ha, N. Y.; Ahn, Y. H.; Park, J.-Y.; Lee, S. Light intensity dependence of organic solar cell operation and dominance switching between Shockley-Read-Hall and bimolecular recombination losses. *Sci. Rep.* **2021**, *11*, 16781.
(53) Galagan, Y.; Coenen, E. W. C.; Zimmermann, B.; Slooff, L. H.; Verhees, W. J. H.; Veenstra, S. C.; Kroon, J. M.; Jørgensen, M.; Krebs, F. C.; Andriessen, R. Scaling Up ITO-Free Solar Cells. *Adv. Energy Mater.* **2014**, *4*, 1300498.
(54) Glowienka, D.; Galagan, Y. Light Intensity Analysis of Photovoltaic Parameters for Perovskite Solar Cells. *Adv. Mater.* **2022**, *34*, 2105920.
(55) Hawash, Z.; Ono, L. K.; Qi, Y. Moisture and Oxygen Enhance Conductivity of LiTFSI-Doped Spiro-MeOTAD Hole Transport Layer in Perovskite Solar Cells. *Adv. Mater. Interfaces* **2016**, *3*, 1600117.
(56) Roesch, R.; Faber, T.; von Hauff, E.; Brown, T. M.; Lira-Cantu, M.; Hoppe, H. Procedures and Practices for Evaluating Thin-Film Solar Cell Stability. *Adv. Energy Mater.* **2015**, *5*, 1501407.
(57) Yan, P.; Yang, D.; Wang, H.; Yang, S.; Ge, Z. Recent Advances in Dopant-Free Organic Hole-Transporting Materials for Efficient, Stable and Low-Cost Perovskite Solar Cells. *Energy Environ. Sci.* **2022**, *15*, 3630−3669.
(58) Pellet, N.; Giordano, F.; Ibrahim Dar, M.; Gregori, G.; Zakeeruddin, S. M.; Maier, J.; Grätzel, M. Hill Climbing Hysteresis of Perovskite-Based Solar Cells: A Maximum Power Point Tracking Investigation. *Prog. Photovoltaics Res. Appl.* **2017**, *25*, 942−950.
(59) Wang, S.; Huang, Z.; Wang, X.; Li, Y.; Günther, M.; Valenzuela, S.; Parikh, P.; Cabreros, A.; Xiong, W.; Meng, Y. S. Unveiling the Role of tBP-LiTFSI Complexes in Perovskite Solar Cells. *J. Am. Chem. Soc.* **2018**, *140*, 16720−16730.
(60) Zheng, L.; Chung, Y.-H.; Ma, Y.; Zhang, L.; Xiao, L.; Chen, Z.; Wang, S.; Qu, B.; Gong, Q. A Hydrophobic Hole Transporting Oligothiophene for Planar Perovskite Solar Cells with Improved Stability. *Chem. Commun.* **2014**, *50*, 11196−11199.
(61) Jeong, M.; Choi, I. W.; Go, E. M.; Cho, Y.; Kim, M.; Lee, B.; Jeong, S.; Jo, Y.; Choi, H. W.; Lee, J.; Bae, J.-H.; Kwak, S. K.; Kim, D. S.; Yang, C. Stable Perovskite Solar Cells with Efficiency Exceeding 24.8% and 0.3-V Voltage Loss. *Science* **2020**, *369*, 1615−1620.

https://doi.org/10.1021/acs.chemmater.3c00145
Chem. Mater. 2023, 35, 2975−2987